1-8-2014

Gas Turbine Engine Behavioral Modeling

Richard T. Meyer
Purdue University, rtmeyer@purdue.edu

Raymond A. DeCarlo
Purdue University, decarlo@purdue.edu

Steve Pekarek
Purdue University, spekarek@purdue.edu

Chris Doktorcik

Gas Turbine Engine Behavioral Modeling

Richard T. Meyer

Raymond A. DeCarlo

Steve Pekarek

Chris Doktorcik

TR-ECE-14-01

January 8, 2014

Purdue University

School of Electrical and Computer Engineering

465 Northwestern Avenue

West Lafayette, IN 47907-1285

Gas Turbine Engine Behavioral Modeling

Richard T. Meyer, Raymond A. DeCarlo, Steve Pekarek, Chris Doktorcik

School of Electrical and Computer Engineering, Purdue University, West Lafayette, IN 47907-1288, USA

Abstract

This paper develops and validates a power flow behavioral model of a gas turbine engine with a gas generator and free power turbine. "Simple" mathematical expressions to describe the engine's power flow are derived from an understanding of basic thermodynamic and mechanical interactions taking place within the engine. The engine behavioral model presented is suitable for developing a supervisory level controller of an electrical power system that contains the engine connected to a generator and a large interconnection of many components, e.g., a naval ship power system powered by gas turbine engines. First principles engine models do not lend themselves to the preceding control development because of their high granularity. The basis of the behavioral model development is the balance of energy flow across engine components; power flow is obtained by taking the time derivative of the energy flow. The behavioral model of a specific engine utilizes constants and empirical fits of power conversion efficiencies obtained from data collected from a high-fidelity engine simulator. Behavioral models for a GE LM2500 and an engine similar to a GE T700 are constructed; the 2-norm normalized error between the simulator and behavioral model outputs for both engines is 3.5% or less.

Keywords: Gas turbine engine, Behavioral model, Power flow Control model, Power management, Energy management, Simulation

Email addresses: rtmeyer@purdue.edu (Richard T. Meyer), decarlo@purdue.edu (Raymond A. DeCarlo), spekarek@purdue.edu (Steve Pekarek)

1. Introduction

Power management of interconnected systems, such as the electrical system on a ship, have become critically important for several reasons: (i) the increasingly high cost of energy necessitating efficient on-board power management strategies in the presence of ramp rates of loads and limitations of modern sources [1, 2], (ii) the increasing use of electronics for advanced weapons systems and a move to more efficient electrical propulsion systems across all vehicle types thereby requiring coordinated power distribution [3], and (iii) the increasing use of electrically-powered automated systems to minimize manual labor also requiring coordinated power management strategies. An impediment to power management control is the interconnection of highly granular first principle models making control design and validation numerically untenable. Recasting first principle subsystem models with reduced order models specific to energy and power flows allows the design, simulation, and validation of power management controllers. See for example [4, 5]. Specifically, with the designed power flow controllers in the loop of the high-order high-granularity model, the system can be simulated to produce input-output response trajectories. These input-output trajectory pairs can then be applied to low granularity system power flow model (with controllers in loop) to retune power flow model parameters allowing for a retuning of the controller parameters. The process is iterated until the controller design achieves its desired purpose for the high level model. See for example [6]. Such controllers might oversee a ship's electrical system in which a turbine-generator pair might be an integral component among a large interconnection of many components or subsystems.

This work develops a supervisory level (low granularity) power flow model (a behavioral model) for a gas turbine engine that drives a generator as part of a ship board power grid suitable for real time MPC (model predictive control). In this context, the exact thermodynamic operating conditions of an engine represent a granularity of secondary priority. Nevertheless, the behavioral model derivation relies on an understanding of the basic thermodynamic

and mechanical interactions taking place within a turbine engine. It is from this understanding that we infer "simple" mathematical expressions to describe the engine's energy and power flow behavior. At this writing, there does not appear to be a reliable power management control oriented model in the literature that is suitable for supervisory MPC design.

To demonstrate the adequacy of this behavioral energy/power flow model, we compare its responses (in simulation) to those from the Gas Turbine Simulation Program (GSP) [7, 8] for an engine similar to a GE T700 and a GE LM2500. The comparisons show that the behavioral model produces minimal response errors thereby supporting the validity of the developed behavioral model.

2. Past Turbine Modeling

It is recognized that several gas turbine engine (GTE) models are available [9, 10, 11, 12, 13, 14]. These models are typically thermo-mechanical (first principle) models of high detail and complexity making their use in control strategy studies highly difficult. An additional snag is the need to have parameter values which often are proprietary or depend on proprietary data. Nevertheless, it is important to review some of the past modeling techniques before developing the behavioral model of this paper.

Walsh and Fletcher in [9] provide an aero-thermal model of a gas turbine engine. Model development depends on relations between pressures, temperatures, and fluid properties. Although the model presented in [9] can be solved in "real-time", it is not readily amenable to real time control, and in particular to model predictive control (MPC) due to its sheer mathematical size and internal iterative solution procedure. An alternate approach is found in Hung in [10] which provides a modeling method that relies on transfer functions. However, the number of parameters to be determined for the model is very large. Camporeale et al. in [11] provide another example of gas turbine engine modeling. Similar to the other two approaches, the proposed modeling approach uses thermodynamic variables and uses different differential equations to describe

the fluid state within the engine. The mathematical size of the technique is again too large and complex to be amenable to efficient real time control such as MPC strategies.

Gas turbine engine models have also been developed for control purposes. Brunell et al. [13] utilizes the aero-engine control model structure from [12] to develop a GTE control model for MPC application. In [12], an empirical control model for a 2-spool turbojet employs second-order transfer functions to describe the low and high pressure spool speeds and algebraic relationships to find the turbine inlet temperature and high compressor discharge total pressure. The fuel flow is the only controllable model input. The model relies upon six parameter curves and ten constants that are fit to output from a more detailed engine model. Brunell et al. [13] applies the previous model structure to a dual rotor, aerodynamically coupled machine with a low pressure rotor system (fan and low-pressure turbine) which feeds a high pressure system (core engine). The model is expanded to include two controllable inputs, fuel flow and exhaust nozzle area, and eight outputs: core spool speed, fan speed, engine pressure ratio, core compressor discharge pressure, core high pressure turbine exit pressure, fan stall margin, core stall margin, and thrust. The control model output deviates up to 22% during transients and 7% during steady-state from a physics-based based component level model over an envelope of operation. Brunell et al. use the control model for a nonlinear model predictive control that tracks a change in output power demand. The control model structure in [12, 13] relies upon numerous fits of data from a detailed engine model.

Hannett et al. [14] proposed a control model for a electrical utility plant gas turbine engine. Steady-state operating maps are used to obtain the gas generator turbine mechanical power, compressor torque, power turbine torque, and exhaust temperature. Modeled dynamics include shaft inertial effects and exhaust temperature lags. Model parameters are determined through engine operation tests that include steady-state running and dynamic load changes.

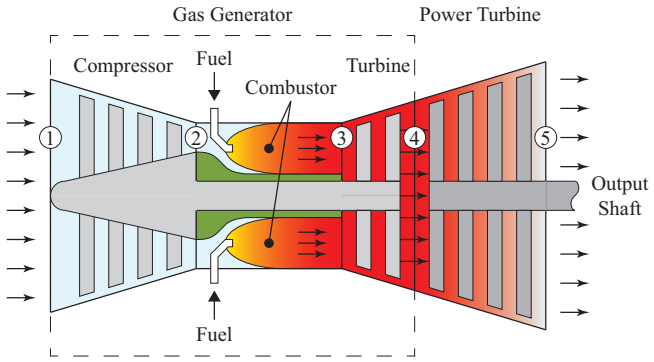

Figure 1: Gas turbine engine diagram with working fluid stations numbered. Ambient air and fuel inputs with power and exhaust gases outputs.

3. Behavioral Gas Turbine Engine Model Overview

The development of these "simple" models of a turbine engine requires the identification of compressor and turbine efficiency maps which are extracted from a high level gas turbine simulation program such as GSP [7, 8] or NPSS [15].

To begin, Fig. 1 illustrates a compartmental view of the gas turbine engine as a machine that converts energy stored in a fuel into usable mechanical energy. The engine is comprised of a gas generator and a free running power turbine. The gas generator itself is composed of three main parts: compressor(s), combustor, and turbine(s); the compressor and turbine may have multiple stages and the assembly comprised of the compressor rotors, turbine rotors, and the common compressor/turbine shaft with rotors is the gas generator spool. The gas generator uses the energy stored in the fuel to create a high temperature, compressed, fast moving output stream of air mixed with combustion products that drives the free power turbine. Specifically, (i) gas generator inlet air is compressed, (ii) the compressed air is mixed with fuel and combusted in the combustor, (iii) a high energy and high temperature gas stream exits the combustor, (iv) a portion of the energy in the gas stream is converted to mechanical energy by the gas generator turbine to drive the compressor, (v) the gas stream is exhausted to the free power turbine, and (vi) a portion of the energy remain-

ing in the gas stream is used to drive the free power turbine whose shaft is available for mechanical work, as would be the case if it were to drive a generator to produce electrical power; the free power turbine's shaft is seen as the "output" shaft of the engine. The free power turbine power extraction from the gas stream depends on its thermodynamic efficiency; the free power turbine is only coupled aerodynamically to the gas generator.

In the next section we argue that for a behavioral model of a turbine engine, the gas generator operational characteristics are not (significantly) coupled to the power turbine rotational speed, i.e. in lieu of a control system that would implicitly couple the combined operation. This is validated in sections 8.3 and 10.3.

Under the condition of (very) weak back-coupling, it is possible to treat the gas generator as an independent "actuator" that drives the free power turbine. The consequence is that the output gas stream of the gas generator acts as an independent input to the free power turbine[1] simplifying modeling.

3.1. Coupling Between Gas Generator and Power Turbine

To argue the validity of the assumption that reverse coupling from the free power turbine to the gas generator is very weak, we cite two sources: Hung [10] and Camporeale et al. [11].

In Hung [10] a gas turbine engine of the form described in section 3 is simulated while driving a three-phase electric generator that undergoes a three-phase fault. During the fault, it is seen that the gas generator speed is smoothly reduced, while the power turbine speed fluctuates wildly, see Fig. 12 of [10]. If there were strong back coupling, the speed fluctuations of the power turbine would have been reflected in a similarly behaved gas generator speed. Since a correlation was not observed, one argues that the power turbine speed at most weakly affects the gas generator operation.

[1] At the thermodynamic level, the independence of the gas generator input is constrained by mass flow and energy matching conditions with the free power turbine.

Furthermore, in Camporeale et al. [11], a GE LM2500 engine is simulated for a varying power load profile. A step load change is simulated and again the gas generator speed is seen to follow a smooth controlled trajectory, whereas the power turbine speed dramatically increases its speed before settling down to a more steady state value as seen in Fig. 12b of [11]. Again if there were strong coupling, the power turbine would have dragged the gas generator speed up, but appears to have at most negligible effect.

In sections 8.3 and 10.3 we use GSP to validate this assumption for the two example engines subject to a square-wave shaped load on the power turbine. Large changes in the power turbine shaft speed as a result of the varying load are not accompanied by similar alterations in gas generator speed.

4. Gas Generator Model Development

4.1. Energy Flow in a Gas Generator

To understand the power flow in the gas generator (the derivative of energy flow), we recognize that all of the energy within the gas generator during normal operation is sourced from fuel entering the combustor. Fig. 2 summarizes the gas generator energy flows. Energy flows in the figure with a superscript "c" can be controlled.

The lower heating value of the fuel, LHV_{fuel}, characterizes the fuel's potential energy. Deviations from the nominal LHV_{fuel} are typically lumped into the combustion efficiency, which is normally estimated to be constant throughout the operating range of the gas generator [16]. As such, in our behavioral model we approximate the energy released from the fuel entering the combustor at any given moment as:

$$E^c_{fuel} = LHV_{fuel} m^c_{fuel} \tag{1}$$

where m^c_{fuel} is the controlled mass of fuel being combusted at any given moment.

Most of E^c_{fuel} is transferred to the working fluid within the combustor. Therefore, in order to describe energy flows, we establish a reference datum energy for the working fluid of the gas generator: we define the energy of the

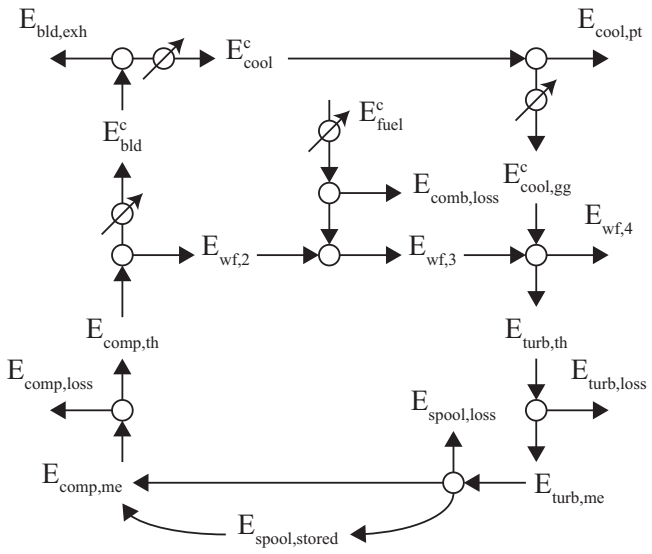

Figure 2: Energy flow diagram for gas generator. Circles indicate energy balance and circles with arrows indicate control valves.

working fluid at the inlet to the compressor to be zero since we assume the majority of the working fluid is atmospheric air, i.e., $E_{wf,1} = 0$ and engine inlet effects are negligible. The notation $E_{wf,i}$ denotes the amount of energy associated with the working fluid (relative to the datum) at number 'i' in Fig. 1 at any given moment. Thus, $E_{wf,2}$ is the energy of the compressed air entering the combustor prior to combustion and $E_{wf,3}$ is the energy of the working fluid immediately post combustion. Finally, $E_{wf,4}$ is the energy of the working fluid leaving the gas generator, which is input to the power turbine.

Using this notation, we set down the energy balance equations pertinent to the gas generator beginning with the combustor:

$$E_{wf,3} - E_{wf,2} = E^c_{fuel} - E_{comb,loss} \tag{2}$$

where $E_{comb,loss}$ is the energy lost due to the inefficiencies of the combustor.

To develop our second energy balance equation we define $E_{comp,th}$ to be the amount of thermodynamic energy transferred to the working fluid by the compression process at any given moment of time. We note that $E_{comp,th}$ is

equal to the mechanical energy used for fluid compression, delivered to the compressor by the gas generator spool, denoted $E_{comp,me}$, minus any losses from mechanical-to-thermodynamic conversion such as from windage [16], denoted as $E_{comp,loss}$. In equation form

$$E_{comp,me} = E_{comp,th} + E_{comp,loss} \tag{3}$$

We define E^c_{bld} as the bleed air energy removed at the compressor exit, typically used for turbine cooling, compressor stall management, or for other purposes [16]. Modeling bleed air as being removed only at the compressor exit, such as in [11, 17], typically results in an adequate representation of engine dynamics. If greater model fidelity is needed, Camporeale et al. [11, 18] suggest augmenting the model with plenums placed between the compressor stages where bleed occurs.

Thus at the compressor-combustor interface

$$E_{wf,2} = E_{comp,th} - E^c_{bld} \tag{4}$$

Moving to the right side of the combustor, we define the thermodynamic energy extracted from the working fluid by the gas generator turbine to be $E_{turb,th}$. Energy balance across the gas generator turbine then satisfies

$$E_{turb,th} = E_{wf,3} + E^c_{cool,gg} - E_{wf,4} \tag{5}$$

where $E^c_{cool,gg}$ is the energy in cooling air (e.g., bleed air) delivered to the turbine. Here, the cooling air is assumed to be mixed with the combustor outflow at the turbine entrance as in [17]. In practice, cooling air is introduced at multiple locations along the gas expansion. In the event that greater model fidelity is needed, additional cooling air injection locations can be treated similarly to the addition of compressor air bleed locations via plenums [11, 18].

A portion of $E_{turb,th}$ will be lost to friction and inefficiencies in the conversion from thermodynamic-to-mechanical energy, denoted as $E_{turb,loss}$. Thus, the mechanical energy available to the spool for transfer to either inertial energy storage or to the compressor is

$$E_{turb,me} = E_{turb,th} - E_{turb,loss} \tag{6}$$

The energy transferred by the spool to the compressor can originate from either the stored energy in the spool or from the turbine or both. Energy balance requires that

$$E_{comp,me} = E_{turb,me} - E_{spool,stored} - E_{spool,loss} \tag{7}$$

where $E_{spool,loss}$ is the mechanical energy losses associated with the rotating spool and

$$E_{spool,stored} = 0.5 J_{spool} \omega_{gg}^2 \tag{8}$$

with ω_{gg} denoting the spool rotational velocity and J_{spool} denoting the mass moment of inertia of the gas generator spool.

Finally, in reference to Fig. 2 the energy balance between bleed air energy and turbine cooling energy is

$$E_{cool}^c + E_{bld,exh} = E_{bld}^c \tag{9}$$

where E_{cool}^c is the total amount of energy taken from the bleed air for turbine cooling and $E_{bld,exh}$ is the energy in the bleed air used for compressor stall management or other purposes. The turbine cooling air energy is routed to the gas generator and free power turbines such that

$$E_{cool,gg}^c + E_{cool,pt} = E_{cool}^c \tag{10}$$

where $E_{cool,pt}$ is any free power turbine cooling air energy.

4.2. Power Flow in a Gas Generator

Time differentiating the energies in Fig. 2, or equivalently Eqs. (1) through (10), produces the governing power equations for the gas generator illustrated by the power flow diagram of Fig. 3. However, direct differentiation does not include efficiency relationships which are common to behavioral models and allow loss terms to be absorbed into the efficiencies. The goal of this section is to differentiate the energy flow equations and incorporate efficiency relationships to

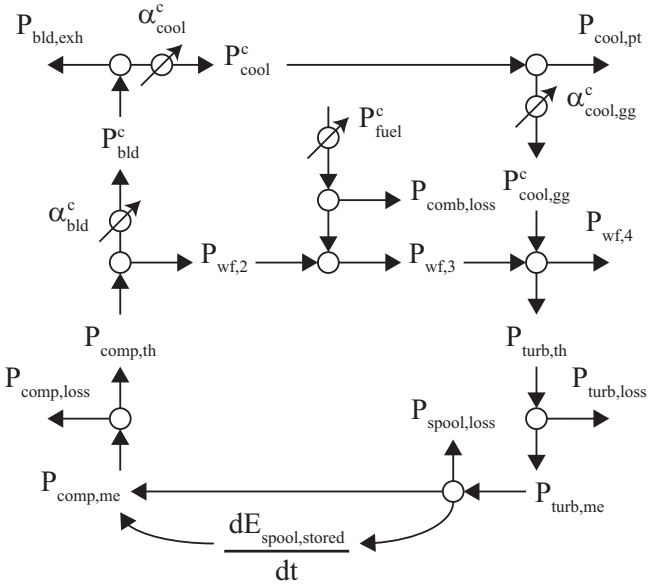

Figure 3: Power flow diagram for gas generator. Circles indicate conservation of power constraints and circles with arrows indicate control valves.

achieve a behavioral power flow model of the gas generator. The set of power flow equations is set forth below:

$$P^c_{fuel} = LHV_{fuel}\frac{dm^c_{fuel}}{dt} = LHV_{fuel}W^c_{fuel} \tag{11}$$

$$P_{wf,3} = \eta_{comb}P^c_{fuel} + (1-\alpha^c_{bld})P_{comp,th} \tag{12}$$

$$P_{comp,th} = \eta_{comp}(P_{comp,me}, \omega_{gg})P_{comp,me} \tag{13}$$

$$P_{turb,th} = \eta_{extract}(P_{wf,3}, P^c_{cool,gg}, \omega_{gg})[P_{wf,3} + P^c_{cool,gg}] \tag{14}$$

$$\begin{aligned} P_{wf,4} =& (1 - \eta_{extract}(P_{wf,3}, P^c_{cool,gg}, \omega_{gg})) \\ & \times [P_{wf,3} + P^c_{cool,gg}] \end{aligned} \tag{15}$$

$$P^c_{cool,gg} = \alpha^c_{cool,gg}\alpha^c_{cool}\alpha^c_{bld}P_{comp,th} \tag{16}$$

$$P_{turb,me} = \eta_{turb}(P_{turb,th}, \omega_{gg})P_{turb,th} \tag{17}$$

$$P_{comp,me} = \eta_{spool}(\omega_{gg})P_{turb,me} - J_{spool}\omega_{gg}\frac{d\omega_{gg}}{dt} \tag{18}$$

$$P_{comp,me} = f_c(P_{turb,me}, \omega_{gg}) \tag{19}$$

Differentiating Eq. (1) results in Eq. (11) where P^c_{fuel} is the power available in the fuel entering the combustor and $dm^c_{fuel}/dt = W^c_{fuel}$ is the instantaneous mass flow rate of the fuel entering the combustor.

In Eq. (12), $P_{wf,3}$ is the net power in the working fluid at the output of the combustor, η_{comb} is the efficiency of combustion, P^c_{fuel} is the power delivered in the fuel, $P_{comp,th}$ is the thermodynamic power in the compressed air input to the combustor, and $\alpha^c_{bld} \in [0, 1]$ is the fraction of compressed air power taken for bleed. Eq. (12) is obtained by (i) taking the time derivative of Eq. (2), (ii) substituting in $\eta_{comb}P^c_{fuel}$ for $P^c_{fuel} - P_{comb,loss}$, (iii) replacing $P_{wf,2}$ with $P_{comp,th} - P^c_{bld}$, and (iv) using $\alpha^c_{bld}P_{comp,th}$ for P^c_{bld}.

Eq. (13) is the mechanical-to-thermodynamic power conversion in the compressor where η_{comp} is the power conversion efficiency and $P_{comp,me}$ is the compressor mechanical power. Eq. (13) results from (i) taking the time derivative of Eq. (3) and (ii) rewriting $P_{comp,me} - P_{comp,loss}$ as an efficiency dependent on $P_{comp,me}$ and ω_{gg} [16].

Next, Eq. (14) provides the gas generator power turbine thermodynamic power extraction from the incoming fluid where $P_{turb,th}$ is the amount of thermodynamic power extracted, $\eta_{extract}$ is the efficiency of the extraction, and $P^c_{cool,gg}$ is the power in cooling air delivered to the turbine. This equation begins with the time derivative of Eq. (5) where $P_{wf,4}$ is the power in the turbine exhaust. In the thermodynamics literature, $P_{turb,th}$ is expressed as a function of input mass flow rate and inlet and outlet temperatures. It is the power in $P_{turb,th}$ required for self sustained operation that determines the drop in temperature across the gas generator turbine since one can view $P_{wf,4}$ as an exhaust term. In turn, this load induced by the compressor on $P_{turb,th}$ can be approximated using the compressor equilibrium running line with input ω_{gg} [19] assuming constant compressor inlet conditions; spool/compressor/turbine losses also depend on ω_{gg}, $P_{wf,3}$, and $P^c_{cool,gg}$. Further, the mass flow rate depends on that generated by the compressor and the combustion process, which depends on ω_{gg} and the upstream variables $P_{wf,3}$ and $P^c_{cool,gg}$. Using these variables, one can approximate the mass flow rate out of the combustion chamber and

the temperature differential which allows us to approximate the gas turbine extraction efficiency denoted $\eta_{extract}$ as a function of $P_{wf,3}$, ω_{gg}, and $P^c_{cool,gg}$. The preceding discussion also leads to Eq. (15). Further, Eq. (16), $P^c_{cool,gg}$ as a function of $P_{comp,th}$ and bleed flow controls, $\alpha^c_{cool}, \alpha^c_{cool,gg} \in [0,1]$, is a result of the power flows shown in Fig. 3.

Turbine thermodynamic-to-mechanical power transfer is given in Eq. (17) where $P_{turb,me}$ is the mechanical power supplied to the spool. Eq. (17) comes from (i) differentiating Eq. (6) and (ii) replacing $P_{turb,th} - P_{turb,loss}$ with $\eta_{turb}(P_{turb,th}, \omega_{gg})P_{turb,th}$; $P_{turb,loss}$ is the power lost to power conversion inefficiencies such as windage. The efficiency depends upon $P_{turb,th}$ and its inlet mass flow rate which depends on ω_{gg} [16].

Eq. (18) is the spool mechanical power balance where η_{spool} accounts for the spool mechanical losses. The equation is obtained from (i) taking the time derivative of Eq. (7), (ii) recognizing the change in stored spool energy is the time derivative of Eq. (8) and substituting, and (iii) replacing $P_{turb,me} - P_{spool,loss}(\omega_{gg})$ with $\eta_{spool}(\omega_{gg})P_{turb,me}$. We note $P_{spool,loss}$ is the power lost in the rotation of the spool from mechanical inefficiencies such as bearing friction and is a function of ω_{gg} [16] and this leads us to η_{spool} as a function of ω_{gg}.

Finally, Eq. (19) is a result of (i) considering the dynamics of $P_{comp,me}$ to be first-order ($dP_{comp,me}/dt = (-P_{comp,me} + f(P_{turb,me}, \omega_{gg}))/\tau$) with a time constant an order of magnitude smaller than the spool [20] and (ii) multiplying the dynamics by τ and applying a singular perturbation.

4.3. Behavioral Dynamics of P^c_{fuel}

The dynamics of P^c_{fuel} stem from the choice of GTE control system. We desire to avoid potentially damaging conditions such as stall and flame-out and to accomplish this, employ the common strategy of enforcing rate limits on P^c_{fuel} [16, 21]. To this end, $\Delta^{inc}_{P,f}$ and $\Delta^{dec}_{P,f}$ are the maximum (absolute) rates at which P^c_{fuel} may increase and decrease, respectively. Between these two limits, we assume that the fuel system possesses a first order behavior with a time constant of τ_{fuel}. Furthermore, let us denote $P^*_{fuel,ss}$ as the desired steady-

state value of P^c_{fuel}, assuming that the short-term load requirement is constant. With these assumptions and definitions, if P^c_{fuel} is moved from one steady-state operating point to another in the least amount of time, then P^c_{fuel} will have the following approximate macro-dynamics:

$$\frac{dP^c_{fuel}}{dt} = \begin{cases} \Delta^{inc}_{P,f}, & \frac{(P^*_{fuel,ss} - P^c_{fuel})}{\tau_{fuel}} > \Delta^{inc}_{P,f} \\ -\Delta^{dec}_{P,f}, & \frac{(P^*_{fuel,ss} - P^c_{fuel})}{\tau_{fuel}} < -\Delta^{dec}_{P,f} \\ \frac{(P^*_{fuel,ss} - P^c_{fuel})}{\tau_{fuel}}, & \text{otherwise} \end{cases} \tag{20}$$

However, Eq. (20) is not everywhere differentiable. Typically for optimization purposes, functions need to be of class $\mathcal{C}^1$. Therefore, for optimization we assume $\Delta^{inc}_{P,f} = \Delta^{dec}_{P,f}$ and approximate Eq. (20) using the hyperbolic tangent function. As such, let us denote $\Delta_{P,f}$ as the maximum absolute rate at which P^c_{fuel} may change. With this definition, we approximate Eq. (20) by:

$$\frac{dP^c_{fuel}}{dt} = \Delta_{P,f} \tanh\left(\frac{P^*_{fuel,ss} - P^c_{fuel}}{\tau_{fuel}\Delta_{P,f}}\right) \tag{21}$$

In the case of $\Delta^{inc}_{P,f} \neq \Delta^{dec}_{P,f}$, hyperbolic tangent functions may be defined on intervals where $P^*_{fuel,ss} - P^c_{fuel} > 0$ and $P^*_{fuel,ss} - P^c_{fuel} < 0$ and then joined together with a function defined around $P^*_{fuel,ss} = P^c_{fuel}$ that maintains $\mathcal{C}^1$ continuity. Subsequent model development is not dependent upon the exact $\mathcal{C}^1$ form of dP^c_{fuel}/dt.

5. Free Power Turbine Model Development

5.1. Energy Flow of a Power Turbine

Fig. 4 shows the energy flows for the free power turbine[2]. The available energy in the working fluid input is denoted by $E_{wf,4}$ as set forth in section 4.1 with $E_{cool,pt}$ being a portion of the bleed air from the compressor which adds an additional energy input. The exhaust energy of the power of the free power

[2]Recall the free power turbine is only aerodynamically coupled to the gas generator.

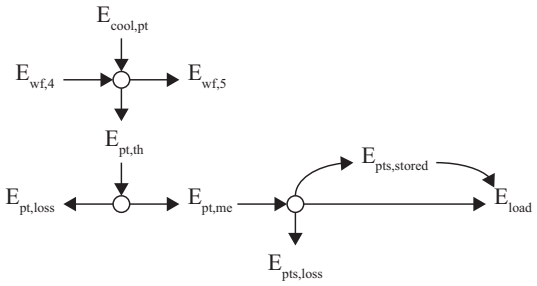

Figure 4: Energy flow diagram for free power turbine.

turbine is $E_{wf,5}$. Finally, $E_{pt,th}$ denotes the thermodynamic energy extracted from the working fluid by the power turbine available for external work. Thus

$$E_{pt,th} = E_{wf,4} + E_{cool,pt} - E_{wf,5} \tag{22}$$

A portion of $E_{pt,th}$ is lost to friction and thermodyamic-to-mechanical inefficiencies and is designated $E_{pt,loss}$. It follows that the mechanical energy available to the shaft for work and/or storage as rotational energy is

$$E_{pt,me} = E_{pt,th} - E_{pt,loss} \tag{23}$$

Finally, denoting E_{out} as the energy transferred to the load through the shaft, $E_{pts,loss}$ as all shaft mechanical energy losses, and $E_{pts,stored} = 0.5 J_{pt} \omega_{PT}^2$ the rotational stored energy, we arrive at the energy balance equation:

$$\begin{aligned} E_{out} &= E_{pt,me} - E_{pts,loss} - E_{pts,stored} \\ &= E_{pt,me} - E_{pts,loss} - 0.5 J_{pt} \omega_{PT}^2 \end{aligned} \tag{24}$$

where J_{pt} is the combined rotational inertia of the free power turbine and the load. Note that $E_{pts,loss}$ may be non-zero even when $E_{pt,me} = 0$ since there are frictional losses associated with the power turbine spinning.

5.2. Power Flow of a Free Power Turbine

Fig. 5 represents the time derivative of Fig. 4 and summarizes the power flows for the free power turbine which analytically are the time derivatives of Eqs. (22)-(24). Similar to section 4.2, the goal here is to produce a behavioral

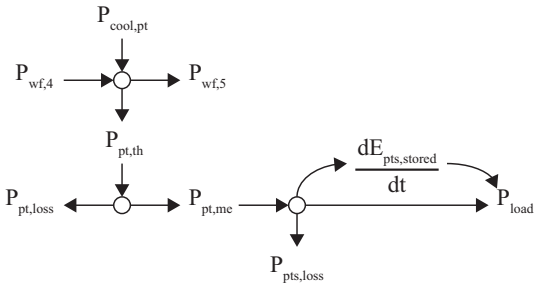

Figure 5: Power flow diagram for free power turbine.

model of the free power turbine by differentiating energy flow equations and then incorporating efficiency relationships. The set of power flow equations are given below:

$$\begin{aligned} P_{pt,th} =& \eta_{extract,pt}(P_{wf,4}, P_{cool,pt}, \omega_{gg}, \omega_{PT}) \\ & \times [P_{wf,4} + P_{cool,pt}] \end{aligned} \tag{25}$$

$$\begin{aligned} P_{wf,5} =& (1 - \eta_{extract,pt}(P_{wf,4}, P_{cool,pt}, \omega_{gg}, \omega_{PT})) \\ & \times [P_{wf,4} + P_{cool,pt}] \end{aligned} \tag{26}$$

$$P_{cool,pt} = (1 - \alpha^c_{cool,gg})\alpha^c_{cool}\alpha^c_{bld}P_{comp,th} \tag{27}$$

$$P_{pt,me} = \eta_{pt}(P_{pt,th}, \omega_{gg}, \omega_{PT})P_{pt,th} \tag{28}$$

$$P_{out} = \eta_{pts}(\omega_{PT})P_{pt,me} - J_{pt}\omega_{PT}\frac{d\omega_{PT}}{dt} \tag{29}$$

Eq. (25) describes the thermodynamic power, $P_{pt,th}$, extracted by the turbine. The equation is obtained by differentiating Eq. (22) and, using reasoning similar to that in section 4.2, simplifying the result with an extraction efficiency, here $\eta_{extract,pt}$. The engine exhaust power, $P_{wf,5}$, Eq. (26), results from substituting the expression for $P_{pt,th}$ in Eq. (25) into the time derivative of Eq. (22) and then solving for $P_{wf,5}$. Eq. (27), the turbine cooling power, $P_{cool,pt}$, is a fraction of the bleed air power from the compressor.

Next, Eq. (28) represents the mechanical power transferred to the shaft, $P_{pt,me}$, which follows from the time derivative of Eq. (23) and the incorporation of a turbine efficiency relationship. Turbine efficiency here depends on its input

power, rotation speed, and inlet mass flow rate, which as before depends on ω_{gg}. Finally, the power transferred to the load, P_{out}, from Eq. (29) is obtained by differentiating Eq. (24) and using an efficiency term, η_{pts}, to account for shaft losses, which are a function of its speed [16].

6. Summary of Behavioral Model of Gas Turbine Engine

Equations(11)-(19), (20), (25)-(29) characterize the behavior of a gas turbine engine. Implementation of models, like the behavioral model, in a MPC structure is greatly improved if the continuous control input to the model is of a normalized form, that is, $u \in [0, 1]$. In the case of the GTE, the control input is the desired quantity of fuel flowing into the combustor at steady-state, $P^*_{fuel,ss}$. Therefore, we express $P^*_{fuel,ss}$ as follows:

$$P^*_{fuel,ss} = (P^{max}_{fuel,ss}(\omega_{PT}) - P^{min}_{fuel,ss}(\omega_{PT}))u_{fuel} + P^{min}_{fuel,ss}(\omega_{PT}) \tag{30}$$

where $u_{fuel} \in [0, 1]$ is the control input and $P^{max}_{fuel,ss}(\omega_{PT})$ and $P^{min}_{fuel,ss}(\omega_{PT})$ are the respective maximum and minimum allowable fuel powers at the current ω_{PT}. The fuel powers can be developed from plots like that shown in Fig. 6[3]. The plots, which are typically provided by manufacturers, have a set of nominal curves which graphically specify the steady-state functional relationship

$$P_{out,ss} = f(P_{fuel,ss}, \omega_{PT,ss}) \tag{31}$$

Graphs similar to Fig. 6 are included in [22] for the AVCO Lycoming TF-40, GE LM2500, and Pratt & Whitney FT4A-14 and FT9. A fuel consumption graph for the Pratt & Whitney FTC-2 is in [23].

The implementation of the developed behavioral model for control of a GTE requires a number of quantities/parameters and efficiencies:

- LHV_{fuel};

[3]Figure 6 was generated using the GSP software TSHAFT example ('TSHAFT_PWinput' model simulated in steady-state, detailed in section 7) that includes a gas generator and free power turbine [7].

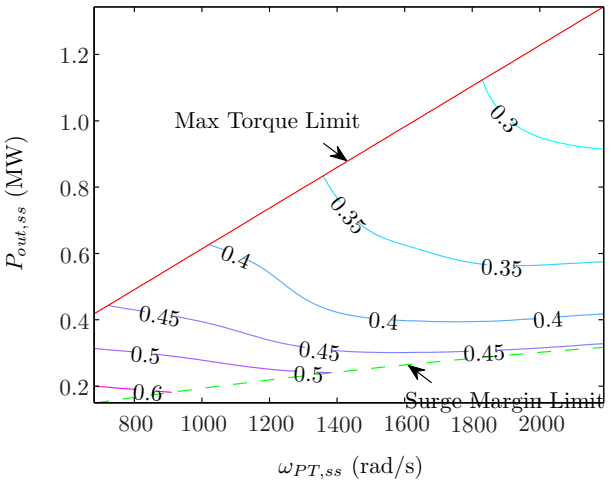

Figure 6: GSP TSHAFT example specific fuel consumption contour plot with contour levels in kg/(kW·hr). 15°C ambient air temperature.

- J_{spool}, the inertia of the gas generator spool;
- J_{pt}, the inertia of the power turbine shaft including connected external load;
- $P_{fuel,ss}^{min}$ and $P_{fuel,ss}^{max}$ as functions of $\omega_{PT,ss}$ (from $P_{out,ss}$);
- the maximum absolute change in fuel power, $\Delta_{P,f}$;
- the fuel system time constant τ_{fuel};
- the respective gas generator combustion, compressor, gas turbine, and gas turbine extraction efficiencies, i.e., η_{comb}, η_{comp}, η_{turb}, and $\eta_{extract}$;
- the spool efficiency, η_{spool};
- $f_c(P_{turb,me}, \omega_{gg})$;
- the free power turbine extraction efficiency, $\eta_{extract,pt}$, the thermodynamic-to-mechanical conversion efficiency, η_{pt}, and the free power turbine shaft efficiency, η_{pts};

Many of the above GTE quantities/parameters are proprietary and must be estimated as scaled versions of values given in the open literature or, in the case of efficiency maps, obtained from curve fitting data from a high fidelity GTE simulator such as GSP [7, 8] and NPSS [15]. Behavioral model parameters for two example engines are developed in subsequent sections.

7. TSHAFT Gas Turbine Engine Behavioral Model Parameter Identification

The GSP [7, 8] is a graphical capture simulator for gas turbine engines. The GSP represents the engine using an underlying thermofluid-mechanical dynamical model; specifically, working fluid properties are averaged over the flow cross sectional areas and thus vary along the axial direction of the engine. There are two stages to creating a GSP model: (i) assembling a graphical representation of the system from a library of generic engine components such as compressors, turbines, combusters, etc., and (ii) entering the component parameters consistent with the engine type.

Several example GSP models are available for download [24]. One such model is the 'TSHAFT_PWinput' model (denoted as TSHAFT-GSP here) that approximates a GE T700 engine which has a configuration consistent with the Gas Turbine Behavioral Model (GTBM) developed herein. Some of the data within TSHAFT-GSP is directly applicable to the GTBM. Other GTBM parameters, including efficiencies, must be extracted from diverse exercises of the TSHAFT-GSP.

Table 1 shows GTBM parameters available directly from TSHAFT-GSP and the others that must be inferred from simulation data: $f_c(P_{comp,me}, \omega_{gg})$, $\eta_{extract}(P_{wf,3}, P^c_{cool,gg}, \omega_{gg})$, $\eta_{extract,pt}(P_{wf,4}, P_{cool,pt}, \omega_{gg}, \omega_{PT})$, $P^{max}_{fuel,ss}(\omega_{PT})$, $P^{min}_{fuel,ss}(\omega_{PT})$, $P_{out,ss}(P_{fuel,ss}, \omega_{PT,ss})$,and $\Delta_{P,f}$. These quantities are functions of $P_{comp,me}$, $P^c_{cool,gg}$, $P_{cool,pt}$, P^c_{fuel}, $P_{wf,3}$, $P_{wf,4}$, ω_{gg}, and ω_{PT}. The exact structure of these functions is unknown. This requires that we presume function structures. It was found that multi-dimensional polynomial forms proved

Table 1: TSHAFT-GSP GTBM parameters (TBE: to be extracted).

Parameter	Value	Parameter	Value
J_{pt}	8.08 kg·m^2	η_{pt}	1
J_{spool}	0.0603 kg·m^2	η_{pts}	0.99
LHV_{fuel}	43.031 MJ/kg	τ_{fuel}	0.03 s
α^c_{bld}	0.0925	f_c	TBE, Sec. 7.1
α^c_{cool}	0.76	$\eta_{extract}$	TBE, Appendix A.1
$\alpha^c_{cool,gg}$	1	$\eta_{extract,pt}$	TBE, Appendix A.2
η_{comb}	0.985	$P^{max}_{fuel,ss}$	TBE, Appendix A.3.1
η_{comp}	1	$P^{min}_{fuel,ss}$	TBE, Appendix A.3.2
η_{spool}	0.99	$P_{out,ss}$	TBE, Appendix A.3
η_{turb}	1	$\Delta_{P,f}$	TBE, Appendix A.3.3

adequate. Each polynomial form is specified with a set of coefficients, c_i. The coefficients are determined as least-squares fits to TSHAFT-GSP data. THSAFT-GSP simulation data included both steady-state and transient responses. The quality of the fit depends not only on the polynomial structure but also on the richness of the data. In steady-state, the THSAFT-GSP operational envelope in ω_{PT} and P_{out} (described shortly) was gridded and all needed TSHAFT-GSP power, speed, fuel values, etc. computed in the GSP simulator. In the transient data collection, responses were computed while fuel was varied and ω_{PT} was held constant. Appropriate subsets of the combined data were used to execute the least-squares fits. The worst coefficient of determination, R^2, obtained was 0.9992, suggesting excellent fits to the TSHAFT-GSP data.

The TSHAFT-GSP P_{out} and ω_{PT} operational envelope is shown in Fig. 6: $\omega_{PT} \in [680.7, 2188.6]$ rad/s where the maximum value is given in TSHAFT-GSP and the minimum is approximately equal to 30% of full speed, the lower limit for a GE T700 in [25]; P_{out} values at a given ω_{PT} range between the P_{out} at the zero surge margin and $P^{max}_{out}(\omega_{PT}) = \omega_{PT} T^{max}_{PT} \cdot 10^{-6}$ MW where

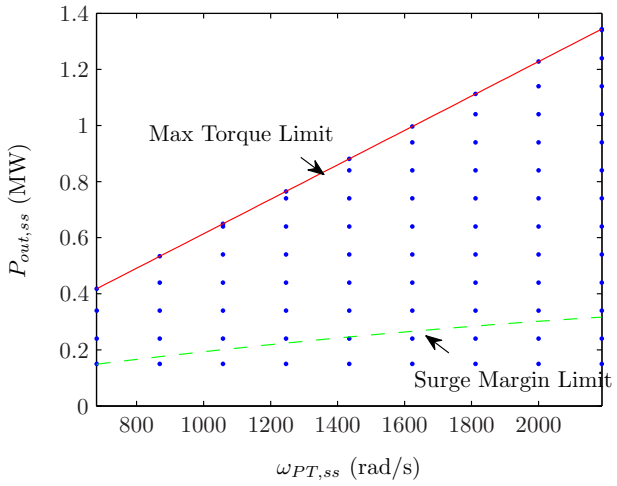

Figure 7: TSHAFT-GSP steady-state solution $(\omega_{PT,ss}, P_{out,ss})$ grid points.

$T_{PT}^{max} = 614$ Nm. Further, Fig. 7 shows the $(\omega_{PT,ss}, P_{out,ss})$[4] grid points for TSHAFT-GSP steady-state data collection: the range of ω_{PT} is divided into eight equal partitions; $P_{out,ss}$ at each $\omega_{PT,ss}$ is the union of $P_{out}^{max}(\omega_{PT,ss})$ and $P_{out,ss}(\omega_{PT,ss}) = \{0.15 + 0.1n \text{ MW} : 0.15 + 0.1n < P_{out}^{max}(\omega_{PT,ss}), n \in \mathbb{Z}_{\geq 0}, \text{surge margin} \geq 0\}$. The use of different $(\omega_{PT,ss}, P_{out,ss})$ points is possible but the ones used here are sufficient for GTBM development as shown in the simulations later on.

TSHAFT-GSP transient data was collected at ω_{PT} values of 680.7, 1434.7, and 2188.6 rad/s using the ω_{PT} specific fuel schedule provided in section 8.1; the fuel input has two step changes over a 20 s simulation. GTBM development is possible with different/additional transient data but the transient data collected appears sufficient as illustrated later.

[4]The subscript 'ss' means steady-state.

7.1. TSHAFT Compressor Power Relationship

To approximate Eq. (19), we use a modified quadratic surface designated by $f_{2,1}$ and specified below:

$$P_{comp,me} = f_c(P_{turb,me}, \omega_{gg}) \cong f_{2,1}(c_{comp,me}, P_{turb,me}, \omega_{gg}) \tag{32}$$

where with $c_{comp,me} = [c_{00}, c_{10}, c_{01}, c_{20}, c_{11}]^T$,

$$f_{2,1}(c_{comp,me}, x, y) = c_{00} + c_{10}x + c_{01}y + c_{20}x^2 + c_{11}xy. \tag{33}$$

A least squares fit found that $c_{comp,me} = [-2.1556 \cdot 10^{-2}, -3.4351, 1.0307 \cdot 10^{-4}, -0.40722, 1.0784 \cdot 10^{-3}]^T$. R^2, SSE, and RMSE fit quality are respectively 0.9998, $2.2389 \cdot 10^{-2}$, and $5.8420 \cdot 10^{-3}$. These values indicate an excellent quality of fit. We note here that alternate fit equations with, for example, higher powers on the variables did not result in significantly improved fit quality.

The other remaining approximations are set forth in Appendix A.

8. TSHAFT Gas Turbine Engine Simulations

Here we compare the transient responses of the TSHAFT-GSP and the GTBM developed in the previous section. Our purpose here is to validate the assumptions used in the development of the GTBM and to show that minimal error results in using the behavioral model, properly parameterized, in typical responses. Thus making the GTBM useful for controller design.

8.1. TSHAFT-GSP and Gas Turbine Engine Behavioral Model Transient Response Simulations

The GTBM is implemented in MATLAB and simulated using the *ode23t* solver; initial conditions for a GTBM simulation are made equal to those of a comparable TSHAFT-GSP simulation. Simulations cover 20 s of operation. Data is sampled at 10 Hz. During each simulation the power turbine speed is held constant at the respective values of 6500 (680.7), 10100 (1057.7), 13700 (1434.7), 17300 (1811.7), and 20900 rpm (2188.6 rad/s). On the other

hand, the GTBM commanded normalized fuel input, u_{fuel}, has a unit step rise and one-half step decrease to simulate severe operation associated with slam acceleration and slam deceleration, respectively [16]:

$$u_{fuel}(t) = \begin{cases} 0, & 0 \text{ s} \leq t < 1 \text{ s} \\ 1, & 1 \text{ s} \leq t < 10 \text{ s} \\ 0.5, & 10 \text{ s} \leq t \leq 20 \text{ s} \end{cases} \tag{34}$$

Unlike the GTBM, the TSHAFT-GSP fuel input is entered as a series of W^c_{fuel}, denoted $W^{c,GSP}_{fuel}$, and time points from which the GSP linearly interpolates the desired fuel flow at a certain time. The $W^{c,GSP}_{fuel}$ and time point data are obtained by (i) performing a continuous-time simulation of Eq. (21) with input from Eq. (30) and u_{fuel} above to obtain P^c_{fuel} over the simulation time, (ii) dividing P^c_{fuel} by LHV_{fuel} to obtain W^c_{fuel}, and (iii) sampling W^c_{fuel} at 10 Hz to get $W^{c,GSP}_{fuel}$. Further, to ensure both the TSHAFT-GSP and GTBM use the same fuel input, GTBM P^c_{fuel} is interpolated from $P^{c,GSP}_{fuel} = W^{c,GSP}_{fuel} LHV_{fuel}$ data.

Figures 8, 9 and 10 compare TSHAFT-GSP and GTBM $P_{comp,th}$, $P_{turb,th}$, and P_{out} at N_{pt} (ω_{PT}) values of 6500 (680.7), 13700 (1434.7), and 20900 rpm (2188.6 rad/s); similar plots are obtained at the other N_{pt} values simulated.

8.2. THAFT-GSP and Gas Turbine Engine Behavioral Model Response Comparisons

Figures 8, 9 and 10 show the GTBM is able to very closely reproduce TSHAFT-GSP results from given initial conditions and fuel commands. This is further confirmed in Fig. 11 which displays the minimal error in GTBM output power. The adequacy of the GTBM is further evaluated using the 2-norm normalized error:

$$E^{2NN}(x_{GTBM}(t), x_{GSP}(t)) = 100 \frac{\|x_{GTBM}(t) - x_{GSP}(t)\|_2}{\|x_{GSP}(t)\|_2} \tag{35}$$

where $x(t)$ denotes the simulation variable time history for comparison. Table 2 summarizes the 2-norm normalized error obtained for the spool speed, N_{gg};

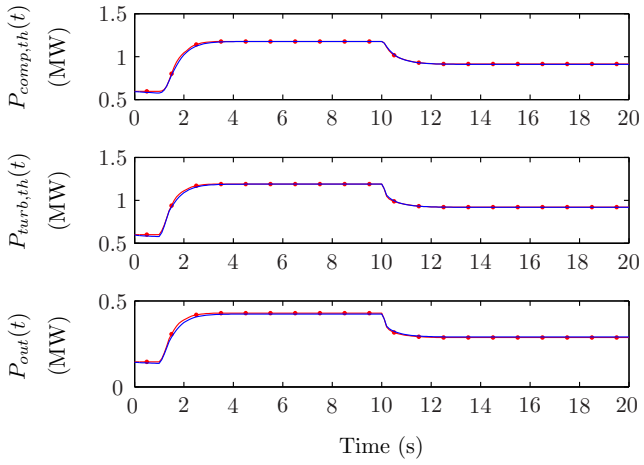

Figure 8: Comparison of TSHAFT-GSP and GTBM simulated power responses at N_{pt} = 6500 rpm (680.7 rad/s): (—) GTBM, (•) GSP.

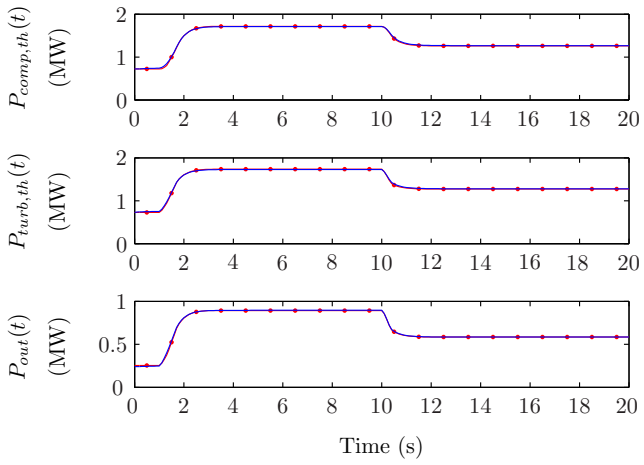

Figure 9: Comparison of TSHAFT-GSP and GTBM simulated power responses at N_{pt} = 13700 rpm (1434.7 rad/s): (—) GTBM, (•) GSP.

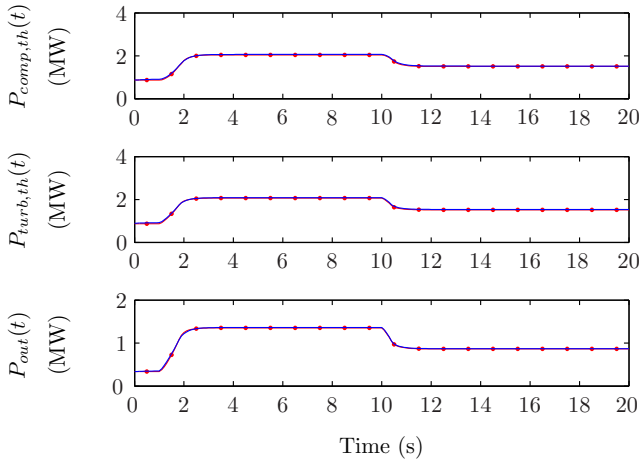

Figure 10: Comparison of TSHAFT-GSP and GTBM simulated power responses at N_{pt} = 20900 rpm (2188.6 rad/s): (—) GTBM, (•) GSP.

Table 2: TSHAFT-GSP and GTBM results 2-norm normalized error.

N_{pt}	ω_{PT}	$E^{2NN}_{N_{gg}}$	$E^{2NN}_{P_{comp,th}}$	$E^{2NN}_{P_{comp,th}}$	$E^{2NN}_{P_{out}}$
6500	680.7	0.23%	0.81%	0.75%	1.75%
10100	1057.7	0.11%	0.40%	0.37%	3.49%
13700	1434.7	0.11%	0.59%	0.66%	0.64%
17300	1811.7	0.21%	0.88%	0.95%	1.22%
20900	2188.6	0.24%	1.17%	1.19%	0.82%

compressor thermodynamic power, $P_{comp,th}$; gas generator turbine thermodynamic power, $P_{turb,th}$; and free power turbine output power, P_{out} obtained for the simulations described in the previous section. Next, Table 3 gives the maximum percent errors (absolute basis) of the GTBM N_{gg}, $P_{comp,th}$, $P_{turb,th}$, and P_{out} values from the corresponding TSHAFT-GSP values over the simulations. Overall, the 2-norm normalized errors are all below 3.5% and the maximum absolute transient errors are below 7.2% which shows that the GTBM is adequate for approximating the high-fidelity THSAFT-GSP output for control design purposes.

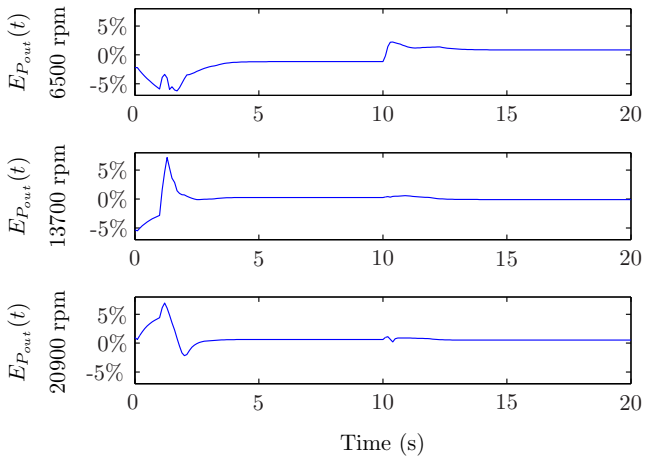

Figure 11: Error between TSHAFT GTBM and GSP $P_{out}(t)$ for N_{pt} of 6500 rpm (680.7 rad/s), 13700 rpm (1434.7 rad/s), and 20900 rpm (2188.6 rad/s).

Table 3: TSHAFT-GSP and GTBM results maximum error.

N_{pt}	ω_{PT}	$E^{max}_{N_{gg}}$	$E^{max}_{P_{comp,th}}$	$E^{max}_{P_{comp,th}}$	$E^{max}_{P_{out}}$
6500	680.7	-1.00%	4.32%	-3.48%	-6.25%
10100	1057.7	-0.21%	3.28%	1.96%	6.87%
13700	1434.7	0.58%	5.20%	3.36%	7.17%
17300	1811.7	0.81%	6.13%	5.1%	5.94%
20900	2188.6	0.84%	5.01%	5.20%	6.93%

8.3. TSHAFT-GSP Check of Gas Turbine Engine Behavioral Model Assumptions

The behavioral model is constructed upon the key assumption of weak back coupling from the power turbine rotor speed, N_{pt}, to the gas generator speed, N_{gg}. To check this assumption, we simulate TSHAFT-GSP over 350 s with a changing load. At the start of the simulation, the engine is at steady-state with a 450 Nm load on the power turbine and fuel supplied at 0.067 kg/s. Then, to test weak back coupling, a square-wave shaped power turbine load is applied from 10 to 190 s with amplitude of 150 Nm, mean of 450 Nm, and period of 60 s; the fuel flow rate remains constant. Fig. 12 shows N_{pt}, N_{gg}, the power turbine input $P_{wf,4}$, and P_{out} normalized to their values at $t = 0$:

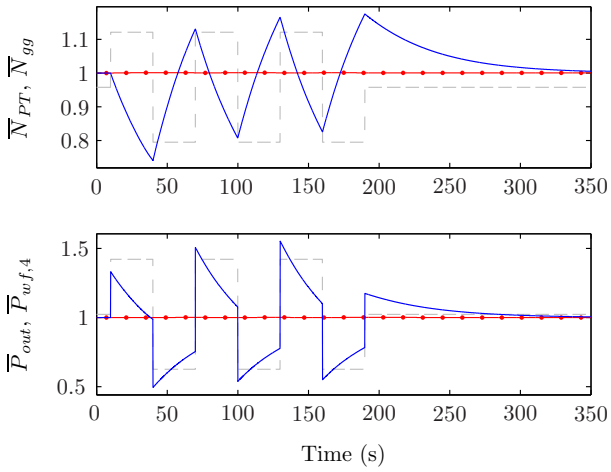

Figure 12: TSHAFT-GSP simulation weak-coupling check with normalized shaft speeds (upper) and normalized power turbine absorbed power and station 4 power (lower): (—) $\overline{N}_{PT}$ (upper)/$\overline{P}_{out}$ (lower), (•) $\overline{N}_{gg}$ (upper)/$\overline{P}_{wf,4}$ (lower), (– –) superimposed power turbine load

$N_{pt} = 14873$ rpm ($\omega_{PT} = 1557.5$ rad/s), $N_{gg} = 41646$ rpm ($\omega_{gg} = 4361.2$ rad/s), $P_{wf,4} = 2.646$ MW, and $P_{out} = 0.701$ MW. N_{pt} varies 45% over the load changes while N_{gg} varies 0.1% and the direction of change is opposite that of N_{pt}. Moreover, the percentage difference in P_{out} is 103%, reflecting the power turbine load and speed changes, but the power supplied to the power turbine, $P_{wf,4}$ is effectively constant with a variation of 0.2%. The results support the assumption of weak back coupling from N_{pt} to the gas generator for this test; when the power turbine load and speed noticeably vary, the gas generator operation is effectively unchanged.

9. Normalized LM2500 Gas Turbine Engine Behavioral Model Parameter Identification

In this section, we present the behavioral model parameters for a GE LM2500 having normalized values (denoted as the normalized LM2500) in consideration of proprietary information: maximum engine power is 1 MW, N_{gg}^{max} and N_{pt}^{max} are 1000 rpm, and the maximum fuel input is 1 kg/s. The GTBM parameters

were obtained from a GSP model with output that approximates the output of a GE LM2500 simulator for $\omega_{gg} \in [82.2, 104.7]$ rad/s ($N_{gg} \in [785, 1000]$ rpm) and $\omega_{PT} \in [29.1, 104.7]$ rad/s ($N_{pt} \in [278, 1000]$ rpm). Our lack of GE simulator bleed air knowledge prevented us from adequately matching outputs from the simulators outside of the given speed ranges. Further, a complete GTBM parameter set was not obtained directly from the GE simulator because its provided engine specifications and output set are limited.

Table 4 lists the normalized LM2500 GTBM parameters and their source. We point out (i) the α_i^c values were set to zero because GE simulator bleed air data was not available and (ii) unity values for η_{comp}, η_{turb}, and η_{pt} are a consequence of using the GSP, and (iii) η_{comb} was taken from TSHAFT-GSP as a typical value. The values and functional forms of $f_c(P_{comp,me}, \omega_{gg})$, $\eta_{extract}(P_{wf,3}, P^c_{cool,gg}, \omega_{gg})$, $\eta_{extract,pt}(P_{wf,4}, P_{cool,pt}, \omega_{gg}, \omega_{PT})$, $P^{max}_{fuel,ss}(\omega_{PT})$, $P^{min}_{fuel,ss}(\omega_{PT})$, and $\Delta_{P,f}$ are provided in Appendix C; they were determined using similar reasoning and methods to that provided for the corresponding TSHAFT GTBM quantities as described in section 7 and Appendix A. The worst coefficient of determination, R^2, obtained was 0.9988, suggesting excellent fit to the GSP data and usefulness of the data fitting approach introduced with the TSHAFT example. However we note that, unlike the TSHAFT example, the data used to obtain $P^{max}_{fuel,ss}(\omega_{PT})$ and $P^{min}_{fuel,ss}(\omega_{PT})$ is taken from the GE simulator and thus $P_{out,ss}(P_{fuel,ss}, \omega_{PT,ss})$ is not required in this example.

Steady-state response GSP data for parameter fitting was generated using the grid of $(\omega_{PT,ss}, P_{out,ss}, W_{fuel,ss})$ input values listed in Appendix B. GSP transient response data was collected at ω_{PT} values of 29.1, 66.9, and 104.7 rad/s using the ω_{PT} specific fuel schedule provided in section 10.1; the fuel input has two step changes over a 20 s simulation. GTBM parameter development is possible with different/additional steady-state and transient data but the data collected is sufficient for GTBM development as shown in the simulations later on.

Table 4: Normalized LM2500 GTBM parameters ([G]: GE simulator, [T]: TSHAFT-GSP, TBE: to be extracted).

Parameter	Value	Parameter	Value
J_{pt}	49.445 kg·m^2 [G]	η_{pt}	1
J_{spool}	39.405 kg·m^2 [G]	η_{pts}	0.99 [17]
LHV_{fuel}	2.7045 MJ/kg [17]	τ_{fuel}	0.2 s [26]
α^c_{bld}	0	f_c	TBE, Appendix C
α^c_{cool}	0	$\eta_{extract}$	TBE, Appendix C
$\alpha^c_{cool,gg}$	0	$\eta_{extract,pt}$	TBE, Appendix C
η_{comb}	0.985 [T]	$P^{max}_{fuel,ss}$	TBE, Appendix C
η_{comp}	1	$P^{min}_{fuel,ss}$	TBE, Appendix C
η_{spool}	0.99 [17]	$\Delta_{P,f}$	TBE, Appendix C
η_{turb}	1		

10. Normalized LM2500 Gas Turbine Engine Simulations

Here we compare the transient responses of the normalized LM2500 GSP model and the developed GTBM. As with the TSHAFT example, our purpose here is to validate the assumptions used in the development of the GTEBM and to show that minimal error results in using the behavioral model, properly parameterized, in typical responses. Thus showing again that the GTBM is useful for controller design.

10.1. Normalized LM2500 Gas Turbine Engine Behavioral Model and GSP Transient Response Simulation

The GTBM is implemented in MATLAB and simulated using the *ode23t* solver; initial conditions for a GTBM simulation are set equal to those of a comparable GSP simulation. Simulations cover 20 s of operation during which data is sampled at 10 Hz. During each simulation power turbine speed is held constant at the respective values of 278 (29.1), 639 (66.9), and 1000 (104.7) rpm (rad/s). However the commanded fuel power has approximately a

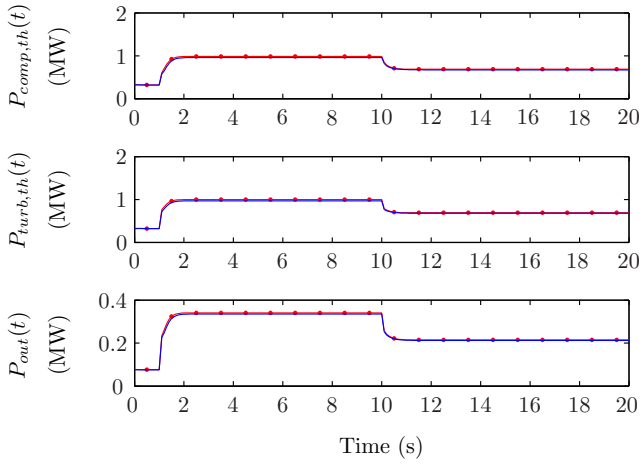

Figure 13: Comparison of normalized LM2500 GSP and GTBM simulated power responses at 278 rpm (29.1 rad/s): (—) gas turbine engine behavioral model, (•) GSP.

step rise and one-half step decrease to simulate severe operation associated with slam acceleration and slam deceleration, respectively [16]:

$$P^c_{fuel}(t) = \begin{cases} P^{min}_{fuel,ss}(\omega_{PT}), & 0 \text{ s} \leq t < 1 \text{ s} \\ P^{min}_{fuel,ss}(\omega_{PT}) + \frac{\Delta_{P_{fuel,ss}}}{0.1}(t-1), & 1 \text{ s} \leq t < 1.1 \text{ s} \\ P^{max}_{fuel,ss}(\omega_{PT}), & 1.1 \text{ s} \leq t < 10 \text{ s} \\ P^{max}_{fuel,ss}(\omega_{PT}) - \frac{\Delta_{P_{fuel,ss}}}{0.2}(t-10), & 10 \text{ s} \leq t \leq 10.1 \text{ s} \\ \frac{P^{min}_{fuel,ss}(\omega_{PT}) + P^{max}_{fuel,ss}(\omega_{PT})}{2}, & 10.1 \text{ s} \leq t \leq 20 \text{ s} \end{cases} \tag{36}$$

where $\Delta_{P_{fuel,ss}} = P^{max}_{fuel,ss}(\omega_{PT}) - P^{min}_{fuel,ss}(\omega_{PT})$. In this example, we bypassed u_{fuel} and utilized $P^c_{fuel}(t)$ directly to simplify the manual entry of the desired fuel input into the GSP. The normalized LM2500 GSP model fuel input is entered as a series of W^c_{fuel}, denoted $W^{c,GSP}_{fuel}$, and time points. The $W^{c,GSP}_{fuel}$ and time point data consist of the values of $P^c_{fuel}(t)$ divided by LHV_{fuel} at $t \in \{0, 1, 1.1, 10, 10.1, 20\}$ s.

Figures 13, 14 and 15 show differences in the $P_{comp,th}$, $P_{turb,th}$, and P_{out} for N_{pt} (ω_{PT}) values of 278 (29.1), 639 (66.9), and 1000 (104.7) rpm (rad/s), respectively.

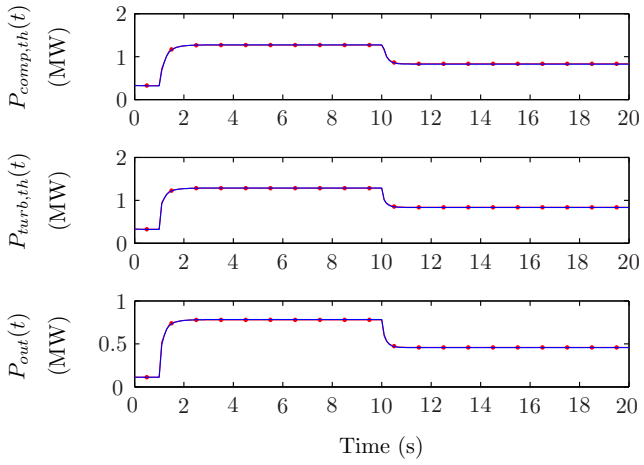

Figure 14: Comparison of normalized LM2500 GSP and GTBM simulated power responses at 639 rpm (66.9 rad/s): (—) gas turbine engine behavioral model, (•) GSP.

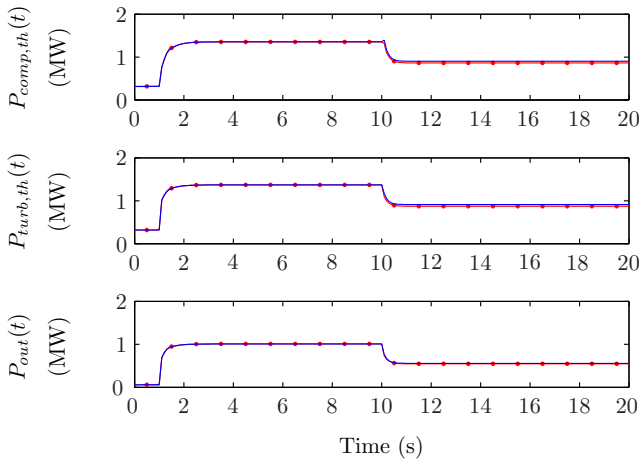

Figure 15: Comparison of normalized LM2500 GSP and GTBM simulated power responses at 1000 rpm (104.7 rad/s): (—) gas turbine engine behavioral model, (•) GSP.

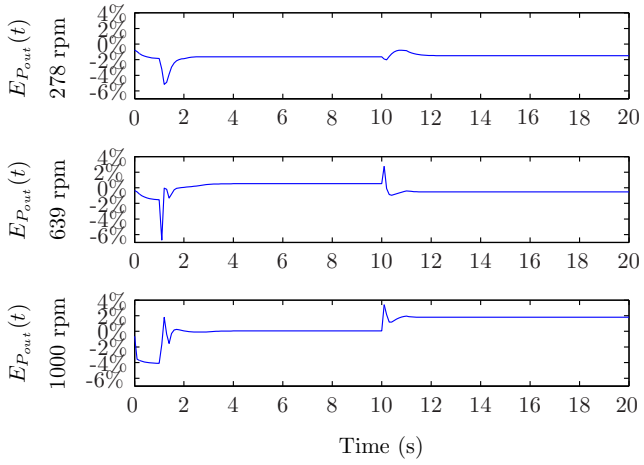

Figure 16: Error between normalized LM2500 GTBM and GSP $P_{out}(t)$ for N_{pt} of 278 rpm (29.1 rad/s), 639 rpm (66.9 rad/s), and 1000 rpm (104.7 rad/s).

10.2. Normalized LM2500 Gas Turbine Engine Behavioral Model and GSP Response Comparisons

Figures 13, 14 and 15 show that the GTBM is able to very closely mimic GSP results from given initial conditions and fuel commands. This is further confirmed in Fig. 16 which displays the overall minimal error in GTBM output power. The adequacy of the GTBM is further evaluated using the 2-norm normalized error calculated using Eq. (35). Table 5 summarizes the 2-norm normalized error obtained for the spool speed, N_{gg}; compressor thermodynamic power, $P_{comp,th}$; gas generator turbine thermodynamic power, $P_{turb,th}$; and free power turbine output power, P_{out} obtained for the simulations described in the previous section. Next, Table 6 shows the maximum percent error difference (absolute basis) of the GTBM N_{gg}, $P_{comp,th}$, $P_{turb,th}$, and P_{out} values from the GSP values over the simulations. Overall, the 2-norm normalized errors are all below 2.7% and the maximum absolute errors are below 7.6% which shows again that the BM is adequate for approximating the high-fidelity GSP model output for control design purposes.

Table 5: Normalized LM2500 behavioral model and GSP results 2-norm normalized error.

N_{pt}	ω_{PT}	$E^{2NN}_{N_{gg}}$	$E^{2NN}_{P_{comp,th}}$	$E^{2NN}_{P_{turb,th}}$	$E^{2NN}_{P_{out}}$
278	29.1	0.55%	2.66%	2.65%	1.71%
639	66.9	0.19%	0.73%	0.53%	0.68%
1000	104.7	0.57%	2.47%	2.50%	0.95%

Table 6: Normalized LM2500 behavioral model and GSP results maximum absolute error.

N_{pt}	ω_{PT}	$E^{max}_{N_{gg}}$	$E^{max}_{P_{comp,th}}$	$E^{max}_{P_{turb,th}}$	$E^{max}_{P_{out}}$
278	29.1	-2.36%	-7.58%	-6.61%	-5.15%
639	66.9	-1.50%	-6.53%	-2.39%	-6.71%
1000	104.7	1.69%	6.13%	6.83%	-4.09%

10.3. Normalized LM2500 GSP Model Check of Gas Turbine Engine Behavioral Model Assumptions

We again check the assumption of weak back coupling from the power turbine rotor speed, N_{pt}, to the gas generator speed, N_{gg}. The form of the test is the same as for the TSHAFT-GSP in section 8.3 where a square-wave shaped power turbine load of period 60 s is applied. For the normalized LM2500 GSP model test, the load has a mean of mean of $4.9761{\cdot}10^3$ Nm and amplitude of $1.2440{\cdot}10^3$ Nm and the fuel is supplied at a constant rate of 0.44441 kg/s. Fig. 17 shows N_{pt}, N_{gg}, the power turbine input $P_{wf,4}$, and P_{out} normalized to their values at $t = 0$: $N_{pt} = 641$ rpm ($\omega_{PT} = 67.1$ rad/s), $N_{gg} = 869$ rpm ($\omega_{gg} = 91.0$ rad/s), $P_{wf,4} = 1.1471$ MW, and $P_{out} = 0.33390$ MW. N_{pt} varies 64% over the load changes while N_{gg} varies 0.9% and the direction of change is opposite that of N_{pt}. Moreover, the percentage difference in P_{out} is 101%, reflecting the power turbine load and speed changes, but the power supplied to the power turbine, $P_{wf,4}$ is effectively constant with a difference of 0.4%. The results support the assumption of weak back coupling from N_{pt} to the gas generator for this test; when the power turbine load and speed noticeably vary, the gas generator operation is effectively unchanged.

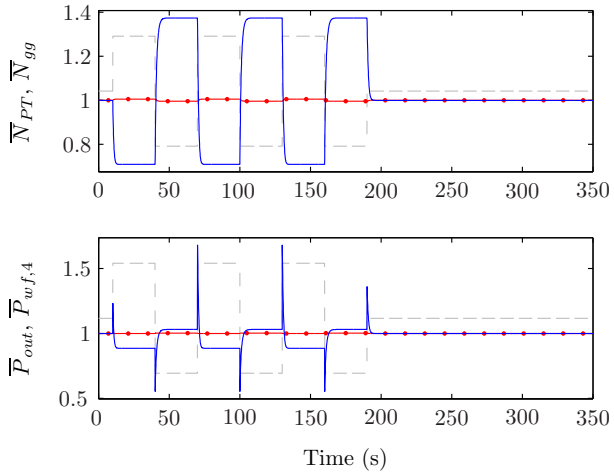

Figure 17: Normalized LM2500 GSP model simulation weak-coupling check with normalized shaft speeds (upper) and normalized power turbine absorbed power and station 4 power (lower): (—) $\overline{N}_{PT}$ (upper)/$\overline{P}_{out}$ (lower), (•) $\overline{N}_{gg}$ (upper)/$\overline{P}_{wf,4}$ (lower), (– –) superimposed power turbine load

11. Conclusions

A gas turbine engine behavioral model for power management control design is derived wherein the engine is composed of a gas generator and free running power turbine. The behavioral model presented has three advantages. First, it is structurally simpler than a detailed first principles engine model and is suitable for control purposes. Second, it requires a low number of surface fits for operational characteristics, reducing the amount of data (particularly proprietary) needed to model the engine compared to other control models. The behavioral models here require three surface fits (compressor power, gas generator turbine extraction efficiency, and free power turbine extraction efficiency). The minimum and maximum fuel power fits provided are not counted since they were created out of convenience and not necessity. In contrast, other control models require between four [14] and six fits [12, 13]. Third, the behavioral model is able to produce sufficiently accurate output using less detailed engine information than a high-fidelity first principles model. The maximum error (absolute basis) at steady-state between the behavioral model and GSP outputs for

the TSHAFT engine is no greater than 7.2% over a wide range of power turbine operation speeds. Similarly, for the normalized LM2500, the maximum error (absolute basis) between the behavioral model and GSP outputs is no greater than 7.6%. The 2-norm normalized errors between GTBM and GSP responses for the TSHAFT and normalized LM2500 were all 3.5% or less. These low error values validate the GTBM as being suitable for control design purposes. Further, the key assumption that the gas generator can be treated as the power turbine actuator was investigated and verified using the GSP TSHAFT and normalized LM2500 examples.

Acknowledgments

We would like to thank The Netherlands National Aerospace Laboratory NLR for providing a GSP license and especially Rob Brink for answering our numerous GSP questions and guiding us through the academic licensing process. Also, we are grateful to GE Aviation for providing an LM2500 simulator. This work is partially supported by the Office of Naval Research.

References

[1] Doerry N. Calculating Surface Ship Energy Usage, Energy Cost, and Fully Burdened Cost of Energy. ASNE Naval Engineers Journal 2013;125(3):87 – 90.

[2] Doerry N. Electric Power Load Analysis. ASNE Naval Engineers Journal 2012;124(4):45 –8.

[3] Doerry N, Moniri K. Specifications and Standards for the Electric Warship. In: Electric Ships Technology Symposium (ESTS), 2013 IEEE. 2013, p. 21 –8.

[4] Meyer RT, DeCarlo RA, Meckl PH, Pekarek S. Hybrid model predictive power management of a fuel-cell battery vehicle. Asian Journal of Control 2013;15(3):1 – 17.

[5] Uthaichana K, DeCarlo RA, Bengea SC, Pekarek S, Žefran M. Hybrid optimal theory and predicitive control for power management in hybrid electric vehicle. Journal of Nonlinear Systems and Applications 2011;2(1 -2):96 – 110.

[6] Landau I, Karimi A. Recursive algorithms for identification in closed loop: a unified approach and evaluation. Automatica 1997;33(8):1499 –523. URL: http://dx.doi.org/10.1016/S0005-1098(97)00061-7.

[7] Visser W. Gas Turbine Simulation at NLR. CEAS Symposium on Simulation Technology 1995;(MOD05).

[8] Visser W, Broomhead M, Kogenhop O, Rademaker E. GSP Technical Manual: Version 11. Tech. Rep. NLR-TR-2010-343; National Aerospace Laboratory; 2010.

[9] Walsh PP, Fletcher P. Gas Turbine Performance. Fairfield, NJ: Blackwell Science Ltd and ASME; 1998.

[10] Hung W. Dynamic simulation of gas-turbine generating unit. IEE Proceedings C: Generation Transmission and Distribution 1991;138(4):342 –50.

[11] Camporeale S, Fortunato B, Mastrovito M. A modular code for real time dynamic simulation of gas turbines in simulink. Journal of Engineering for Gas Turbines and Power 2006;128(3):506 –17. URL: http://dx.doi.org/10.1115/1.2132383.

[12] Shaoji Z. A Simplified Real-Time Engine Model for Developing Aeroengine Control System. AIAA 92-3321 1992;.

[13] Brunell B, Bitmead R, Connolly A. Nonlinear model predictive control of an aircraft gas turbine engine. 41st IEEE Conference on Decision and Control 2002;4:4649 –51. URL: http://dx.doi.org/10.1109/CDC.2002.1185111.

[14] Hannett LN, Jee G, Fardanesh B. A Governor/Turbine Model For a Twin Shaft Combustion Turbine. IEEE Transactions on Power Systems 1995;1(1):133 –40.

[15] Lytle JK. The Numerical Propulsion System Simulation: A Multidisciplinary Design System for Aerospace Vehicles. Tech. Rep. NASA/TM-1999-209194; NASA; 1999.

[16] Walsh PP, Fletcher P. Gas Turbine Performance. 2nd. ed.; Fairfield, NJ: Blackwell Science Ltd and ASME; 2004.

[17] Haglind F, Elmegaard B. Methodologies for Predicting the Part-Load Performance of Aero-Derivative Gas Turbines. Energy 2009;34:1484 –92.

[18] Camporeale S, Fortunato B. Performance of a Mixed Gas-Steam Cycle Power Plant Obtained Upgrading an Aeroderivative Gas Turbine. Energy Conversion and Management 1998;39:1683 –92.

[19] Saravanamuttoo HIH, Rogers GFC, Cohen H, Straznicky P. Gas Turbine Theory. 6th ed. ed.; United Kingdom: Pearson Hall; 2008.

[20] Thomas P. Simulation of Industrial Processes for Control Engineers. 1st. ed.; Oxford, England: Butterworth-Heinemann; 1999. ISBN 0-7506-4161-4.

[21] de Jager B. Rotating Stall and Surge Control: A Survey. In: Proceedings of the 34th IEEE Conference on Decision and Control; vol. 2. 1995, p. 1857 –62. doi:10.1109/CDC.1995.480612.

[22] Saarlas M. Steam and Gas Turbines for Marine Propulsion. Annapolis, MD: Naval Institute Press; 1978.

[23] Woodward JB. Marine Gas Turbines. New York, NY: Wiley; 1975.

[24] National Aerospace Laboratory of the Netherlands (NLR) . GSP Sample Models. Available online http://www.gspteam.com/downloads/sample-models; 2013.

[25] United States Army Aviation Warfighting Center . UH-60A T700 Engine 4743-7. Online; 2013. URL: http://www.aasf1-ny.org/4-Standards/Documents/PUBLICATIONS/StudentHandouts/UH60A%20T700%20Engine.pdf.

[26] Doktorcik C. Modeling and simulation of a hybrid ship power system. Master's thesis; Purdue University; West Lafayette, IN; 2011.

Appendix A. TSHAFT GTBM Parameter Functional Fits

Appendix A.1. Gas Generator Turbine Extraction Efficiency

The efficiency, $\eta_{extract}$, in Eq. (14) is the ratio of gas generator turbine thermodynamic output power to thermodynamic input power. The output power is approximated by a modified quadratic equation, labeled $f_{2,1}$. The fit, specified by Eq. (A.1), requires TSHAFT-GSP values for $P^c_{cool,gg}$, $P_{wf,3}$, and ω_{gg}. ω_{gg} is a TSHAFT-GSP native output as are $P_{comp,th}$ and W^c_{fuel}. Thus $P^c_{cool,gg}$ is computed from Eq. (16) using the fractional values in Table 1 and $P_{comp,th}$. $P_{wf,3}$ is from Eq. (12), Table 1, $P_{comp,th}$, and P^c_{fuel} where P^c_{fuel} is calculated with Eq. (11), W^c_{fuel}, and Table 1. As such,

$$\eta_{extract}(P_{wf,3}, P^c_{cool,gg}, \omega_{gg}) \approx \frac{f_{2,1}(c_{extract}, P_{wf,3} + P^c_{cool,gg}, \omega_{gg})}{P_{wf,3} + P^c_{cool,gg}} \tag{A.1}$$

where $c_{extract} = [c_{00}, c_{10}, c_{01}, c_{20}, c_{11}]^T$ and

$$f_{2,1}(c_{extract}, x, y) = c_{00} + c_{10}x + c_{01}y + c_{20}x^2 + c_{11}xy. \tag{A.2}$$

Using least squares to fit $f_{2,1}$ to TSHAFT-GSP $P_{turb,th}$ data, $c_{extract} = [-1.2496, -8.9507 \cdot 10^{-2}, 3.9566 \cdot 10^{-4}, -9.8035 \cdot 10^{-3}, 8.1537 \cdot 10^{-5}]^T$ with R^2=0.9997, SSE=$2.9499 \cdot 10^{-2}$, and RMSE=$6.7058 \cdot 10^{-3}$. It was observed that fits with higher order surface fits showed no noticeably better quality.

Appendix A.2. Free Power Turbine Extraction Efficiency

The efficiency $\eta_{extract,pt}(\omega_{gg}, P_{wf,4}, \omega_{PT})$[5] in Eq. (25) is the fraction of the thermodynamic input power to the free power turbine that is extracted for conversion to mechanical output power. The thermodynamic power extracted by the free power turbine is approximated by a three-dimensional quadratic

[5] $P_{cool,pt}$ is not considered in TSHAFT-GSP and not included in the listed dependencies.

function, denoted $f_{2,2,2}$. The fit set forth in Eq. (A.3) requires TSHAFT-GSP data for ω_{gg}, ω_{PT}, and $P_{wf,4} = P_{wf,3} + P^c_{cool,gg} - P_{turb,th}$ (from Eqs. (14) and (15)); using Appendix A.1 to obtain $P_{wf,3}$ and $P^c_{cool,gg}$ and the native GSP outputs ω_{gg}, ω_{PT}, and $P_{turb,th}$, the fit is

$$\eta_{extract,pt}(P_{wf,4}, \omega_{gg}, \omega_{PT}) \approxeq \frac{f_{2,2,2}(c_{extract,pt}, \omega_{gg}, P_{wf,4}, \omega_{PT})}{P_{wf,4}} \tag{A.3}$$

where $c_{extract,pt} = [c_{000}, c_{100}, c_{010}, c_{001}, c_{110}, c_{101}, c_{011}, c_{111}, c_{200}, c_{020}, c_{002}]^T$ and

$$\begin{aligned} f_{2,2,2}(c_{extract,pt}, x, y, z) =& c_{000} + c_{100}x + c_{010}y + c_{001}z + c_{110}xy \\ &+ c_{101}xz + c_{011}yz + c_{111}xyz \\ &+ c_{200}x^2 + c_{020}y^2 + c_{002}z^2 \end{aligned} \tag{A.4}$$

The least squares fit of $f_{2,2,2}$ to TSHAFT-GSP $P_{pt,th}$ data results in $c_{000} = -0.98485$, $c_{100} = 4.7740 \cdot 10^{-4}$, $c_{010} = -0.53370$, $c_{001} = 7.4699 \cdot 10^{-6}$, $c_{110} = 1.7980 \cdot 10^{-4}$, $c_{101} = 4.8897 \cdot 10^{-9}$, $c_{011} = 1.0773 \cdot 10^{-5}$, $c_{111} = 1.8968 \cdot 10^{-8}$, $c_{200} = -5.9701 \cdot 10^{-8}$, $c_{020} = -3.7386 \cdot 10^{-2}$, $c_{002} = -4.7685 \cdot 10^{-8}$ and a fit quality of R^2=0.9998, SSE=$1.8703 \cdot 10^{-2}$, and RMSE=$5.3193 \cdot 10^{-3}$, which as before is adequate for our needs.

Appendix A.3. TSHAFT Fuel Power Relationships

From steady-state TSHAFT-GSP data, $P_{out,ss} = f(P_{fuel,ss}, \omega_{PT,ss})$ is approximated by $f_{2,2}$:

$$\begin{aligned} P_{out,ss} &= f(P_{fuel,ss}, \omega_{PT}) \\ &\approxeq f_{2,2}(c_{P_{out,ss}}, P_{fuel,ss}, \omega_{PT,ss}, \omega^{min}_{PT,ss}, \omega^{max}_{PT,ss}, \omega^{0}_{PT,ss}) \end{aligned} \tag{A.5}$$

with $c_{P_{out,ss}} = [c_1, c_2, c_3, c_4, c_5, c_6, c_7, c_8, c_9, c_{10}]^T$ and for arbitrary x,

$$f_{2,2}(c_{P_{out,ss}}, x, y, y_{min}, y_{max}, y_0) = \begin{cases} f^1_{2,2}(c_{P_{out,ss}}, x, y, y_{min}, y_{max}, y_0), \\ \qquad\qquad y_{min} \leq y < y_0 \\ f^2_{2,2}(c_{P_{out,ss}}, x, y, y_{min}, y_{max}, y_0), \\ \qquad\qquad y_0 \leq y \leq y_{max} \end{cases} \tag{A.6}$$

$$\begin{aligned} f^1_{2,2}(c_{P_{out,ss}}, x, y, y_{min}, y_{max}, y_0) =& (c_1 + c_2 x + c_3 x^2) y \\ &+ (c_4 x + c_5 x^2) y^2 \\ f^2_{2,2}(c_{P_{out,ss}}, x, y, y_{min}, y_{max}, y_0) =& (c_6 + c_7 x + c_8 x^2) y \\ &+ (c_9 x + c_{10} x^2) y^2 \end{aligned}$$

and $f^1_{2,2} = f^2_{2,2}$ at $y = y_0$ for arbitrary x to prevent jump discontinuities in the approximation. The forms of $f^1_{2,2}$ and $f^2_{2,2}$ are the same as the fit developed in [26] for the AVCO Lycoming TF-40, and the Pratt & Whitney FT4A-14, FT9, and FT4C-2 engines which resulted in $R^2 \geq 0.9997$. Our use of the same general fit surface here as in [26] and continuity of the surfaces at (x, y_0) allows us to develop the minimum and maximum fuel power curves called for in section 6 in essentially the same way as in [26].

To obtain a least squares fit, we first set $\omega^{min}_{PT,ss} = 680.7$ rad/s and $\omega^{max}_{PT,ss} = 2188.6$ rad/s as specified in section 7. The value of $\omega^0_{PT,ss} = 1057.7$ rad/s was chosen via iteration to obtain an adequate R^2=0.9992, SSE=$4.4694 \cdot 10^{-3}$, and RMSE=$8.1674 \cdot 10^{-3}$. The resulting least squares coefficients are $c_{P_{out,ss}} = [-1.8946 \cdot 10^{-4}, 4.0396 \cdot 10^{-4}, 3.4151 \cdot 10^{-5}, -1.0229 \cdot 10^{-7}, -4.5277 \cdot 10^{-8}, -1.8946 \cdot 10^{-4}, 3.8882 \cdot 10^{-4}, -2.3113 \cdot 10^{-5}, -8.7985 \cdot 10^{-8}, 8.8648 \cdot 10^{-9}]^T$. Higher order approximations showed no significant improvement.

Appendix A.3.1. Maximum Fuel Power Function

The maximum steady-state fuel power curve, $P^{max}_{fuel,ss}(\omega_{PT,ss})$, is required in Eq. (30). We approximate $P^{max}_{fuel,ss}(\omega_{PT,ss})$ with a third-order polynomial:

$$P^{max}_{fuel,ss} \approxeq f_3(c_{P^{max}_{fuel,ss}}, \omega_{PT,ss}) \tag{A.7}$$

where $c_{P^{max}_{fuel,ss}} = [c_{11}, c_{12}, c_{13}, c_{14}]^T$ and $f_3(c_{P^{max}_{fuel,ss}}, x) = c_{11} + c_{12}x + c_{13}x^2 + c_{14}x^3$. The fit is similar to what was done in [26].

Values of $P^{max}_{fuel,ss}$ for the $\omega_{PT,ss}$ were obtained by (i) recalling from section 7 that the maximum $P_{out,ss}$ at each $\omega_{PT,ss}$ is equal to $\omega_{PT,ss} T^{max}_{PT} \cdot 10^{-6}$ MW and (ii) solving Eq. (A.5) for $P_{fuel,ss}$ in terms of $(\omega_{PT,ss}, P_{out,ss})$ with the quadratic formula resulting in

$$\begin{aligned} P_{fuel,ss}(c_{P_{out,ss}}, P_{out,ss}, \omega_{PT,ss}) &= -\frac{-c_2\omega_{PT,ss} - c_4\omega^2_{PT,ss} + \sqrt{\Delta}}{2c_3\omega_{PT,ss} + 2c_5\omega^2_{PT,ss}} \\ \Delta &= (c_2\omega_{PT,ss} + c_4\omega^2_{PT,ss})^2 \\ &\quad - 4(c_3\omega_{PT,ss} + c_5\omega^2_{PT,ss})(c_1\omega_{PT,ss} - P_{out,ss}) \end{aligned} \tag{A.8}$$

where $c_1, \ldots, c_5$ values are from Appendix A.3, valid for $\omega_{PT,ss} \in [\omega^{min}_{PT,ss}, wptss^0)$, and $[c_1, \ldots, c_5]^T$ are replaced with $[c_6, \ldots, c_{10}]^T$, respectively, when $\omega_{PT,ss} \in [\omega^0_{PT,ss}, \omega^{min}_{PT,ss}]$. The positive square root is chosen so that the results of Eq. (A.8) are consistent with the output of Eq. (A.5).

Given the $P^{max}_{fuel,ss}$ and $\omega_{PT,ss}$ data, a least squares fit with Eq. (A.7) gave $c_{P^{max}_{fuel,ss}} = [-0.43201, 5.7345 \cdot 10^{-3}, -2.9075 \cdot 10^{-6}, 5.9909 \cdot 10^{-10}]^T$ with good fit quality of R^2=0.9953, SSE=$1.8441 \cdot 10^{-2}$, and RMSE=$6.0730 \cdot 10^{-2}$. Higher order polynomials may be used for the function approximation but f_3 proved acceptable. Further, Eq. (A.7) can be used with ω_{PT} input instead of $\omega_{PT,ss}$ as in Eq. (30) during transient operation.

Appendix A.3.2. Minimum Fuel Power Function

Eq. (30) requires $P^{min}_{fuel,ss}(\omega_{PT,ss})$ which we approximate (as in [26]) with a cubic polynomial:

$$P^{min}_{fuel,ss} \approxeq f_3(c_{P^{min}_{fuel,ss}}, \omega_{PT,ss}) \tag{A.9}$$

where $c_{P^{min}_{fuel,ss}} = [c_{15}, c_{16}, c_{17}, c_{18}]^T$, $f_3(c_{P^{min}_{fuel,ss}}, x) = c_{15} + c_{16}x + c_{17}x^2 + c_{18}x^3$. The values of $P^{min}_{fuel,ss}(\omega_{PT,ss})$ were obtained from Eq. (A.8) with $P_{out,ss}$ set equal to the output power on the zero surge margin curve at $\omega_{PT,ss}$ (see Fig. 6); the values used in this approximation were obtained from interpolation of TSHAFT-GSP surge margin data in section 7. This resulted in $c_{P^{min}_{fuel,ss}} =$

$[0.64373, 1.1950{\cdot}10^{-3}, -6.5999{\cdot}10^{-7}, 1.6020{\cdot}10^{-10}]^T$ with R^2=0.9984, SSE=$3.8511{\cdot}10^{-3}$, and RMSE=$6.3337{\cdot}10^{-3}$. Clearly, a cubic fit was sufficient for our purposes. Again, Eq. (A.9) can be used (approximately) with ω_{PT} input instead of $\omega_{PT,ss}$ as in Eq. (30) during transient operation.

Appendix A.3.3. TSHAFT Maximum Absolute Change in Fuel Power

TSHAFT $\Delta_{P,f}$=3.288 MW/s. It is obtained from

$$\Delta_{P,f} = \frac{\max_{\omega_{PT}\in[\omega_{PT}^{min},\omega_{PT}^{max}]} P_{fuel,ss}^{max} - \min_{\omega_{PT}\in[\omega_{PT}^{min},\omega_{PT}^{max}]} P_{fuel,ss}^{min}}{\Delta t} \quad \text{(A.10)}$$

where the numerator is calculated from the expressions for $P_{fuel,ss}^{max}$ (Eq. (A.7)) and $P_{fuel,ss}^{min}$ (Eq. (A.9)). The value of Δt is chosen as 1 s. This is an average value in [26], since Δt is not available from TSHAFT-GSP data. Estimates of the fuel power rates for the engines listed in Appendix A.3 are set forth in [26].

Appendix B. Normalized LM2500 Model GSP Inputs

The GSP inputs for normalized LM2500 steady-state response were obtained from the GE simulator using inputs of ω_{PT} and ω_{gg} where each $\omega_{PT} \in \{29.1, 34.9, 58.2, 81.5, 104.7\}$ rad/s value was paired with ω_{gg} values of 82.2, 90.5, 98.6, and 104.7 rad/s[6] Thus, the normalized LM2500 GSP model $(\omega_{PT,ss}, P_{out,ss}, W_{fuel,ss})$ inputs for steady-state operation were (104.7,1,1), (81.5,0.91540,0.96677), (58.2,0.67721,0.82251), (104.7,0.82402,0.83687), (81.5,0.75813,0.80952), (58.2,0.64234,0.78354), (34.9,0.40557,0.68098), (29.1,0.33757,0.65295), (104.7,0.36652,0.468343), (81.5,0.35459,0.45535), (58.2,0.31376,0.43689), (34.9,0.22994,0.41570), (29.1,0.20060,0.41160), (104.7,$6.2735{\cdot}10^{-2}$,0.22426), (81.5,0.10149,0.23041), (58.2,0.10706,0.22631), (34.9,$8.3906{\cdot}10^{-2}$,0.21332), and (29.1,$7.3536{\cdot}10^{-2}$,0.20785).

Appendix C. Normalized LM2500 Parameter Functional Fits

The normalized LM2500 parameter functional fits were performed using similar reasoning and methods to that provided for the corresponding TSHAFT

[6] GE simulator output for the $(\omega_{PT}, \omega_{gg})$ pairs of (29.1, 104.7) rad/s and (34.9, 104.7) rad/s indicated these were not valid operating points.

GTBM quantities as described in section 7 and Appendix A.

The approximation of the normalized LM2500 compressor power relationship, Eq. (19), is

$$P_{comp,me} = f_c(P_{turb,me}, \omega_{gg}) \cong f_{4,2}(c_{comp,me}, P_{turb,me}, \omega_{gg}) \tag{C.1}$$

where

$$\begin{aligned} f_{4,2}(c_{4,2}, x, y) =& c_{00} + c_{10}x + c_{01}y + c_{20}x^2 + c_{11}xy \\ &+ c_{02}y^2 + c_{30}x^3 + c_{21}x^2y + c_{12}xy^2 \\ &+ c_{40}x^4 + c_{31}x^3y + c_{22}x^2y^2 \end{aligned} \tag{C.2}$$

and $c_{4,2} = [c_{00}, c_{10}, c_{01}, c_{20}, c_{11}, c_{02}, c_{30}, c_{21}, c_{12}, c_{40}, c_{31}, c_{22}]^T$. The data fit results in $c_{comp,me} = c_{4,2}$ with $c_{00} = -2.8920$, $c_{10} = 18.966$, $c_{01} = 4.7536 \cdot 10^{-2}$, $c_{20} = -22.001$, $c_{11} = -0.25368$, $c_{02} = -1.8980 \cdot 10^{-4}$, $c_{30} = 15.960$, $c_{21} = 0.16012$, $c_{12} = 6.1996 \cdot 10^{-4}$, $c_{40} = 2.2229$, $c_{31} = -0.22689$, $c_{22} = 1.1867 \cdot 10^{-3}$ and fit quality of R^2=0.9996, SSE=$3.6792 \cdot 10^{-3}$,and RMSE=$5.8367 \cdot 10^{-3}$.

The approximation of $\eta_{extract}$ in Eq. (14) for the normalized LM2500 is

$$\eta_{extract}(P_{wf,3}, \omega_{gg}) \cong \frac{f_{4,2}(c_{extract}, P_{wf,3}, \omega_{gg})}{P_{wf,3}} \tag{C.3}$$

where Eq. (C.2) describes $f_{4,2}$. The data fit results in $c_{extract} = c_{4,2}$ with $c_{00} = -10.881$, $c_{10} = 10.129$, $c_{01} = 0.13831$, $c_{20} = -2.9768$, $c_{11} = -0.13290$, $c_{30} = 0.19673$, $c_{21} = 4.5707 \cdot 10^{-2}$, $c_{40} = 2.1652 \cdot 10^{-2}$, $c_{31} = -5.1020 \cdot 10^{-3}$, $c_{02} = c_{12} = c_{22} = 0$ and fit quality of R^2=0.9988, SSE=$1.2516 \cdot 10^{-2}$, and RMSE=$1.0619 \cdot 10^{-2}$.

The approximation of $\eta_{extract,pt}$ in Eq. (25) for the normalized LM2500 is

$$\eta_{extract,pt}(P_{wf,4}, \omega_{gg}, \omega_{PT}) \cong \frac{f_{2,4,2}(c_{extract,pt}, \omega_{gg}, P_{wf,4}, \omega_{PT})}{P_{wf,4}} \tag{C.4}$$

where $c_{extract,pt} = [c_{000}, c_{100}, c_{010}, c_{001}, c_{110}, c_{101}, c_{011}, c_{111}, c_{200}, c_{020}, c_{002}, c_{210},$

$c_{201}, c_{120}, c_{021}, c_{102}, c_{012}, c_{220}, c_{202}, c_{022}, c_{030}, c_{130}, c_{031}, c_{040}]^T$ and

$$\begin{aligned} f_{2,4,2}(c_{extract,pt}, x, y, z) &= c_{000} + c_{100}x + c_{010}y + c_{001}z + c_{110}xy \\ &+ c_{101}xz + c_{011}yz + c_{111}xyz + c_{200}x^2 + c_{020}y^2 + c_{002}z^2 \\ &+ c_{210}x^2y + c_{201}x^2z + c_{120}xy^2 + c_{021}y^2z + c_{102}xz^2 + c_{012}yz^2 \\ &+ c_{220}x^2y^2 + c_{202}x^2z^2 + c_{022}y^2z^2 + c_{030}y^3 + c_{130}xy^3 \\ &+ c_{031}y^3z + c_{040}y^4 \end{aligned} \tag{C.5}$$

The data fit results in $c_{000} = 0$, $c_{100} = 3.2715 \cdot 10^{-3}$, $c_{010} = 5.0458$, $c_{001} = -0.19454$, $c_{110} = -0.10516$, $c_{101} = 4.4157 \cdot 10^{-3}$, $c_{011} = -4.0134 \cdot 10^{-2}$, $c_{111} = 4.9516 \cdot 10^{-4}$, $c_{200} = -5.3809 \cdot 10^{-5}$, $c_{020} = -0.95824$, $c_{002} = 1.1073 \cdot 10^{-3}$, $c_{210} = 5.6633 \cdot 10^{-4}$, $c_{201} = -2.4498 \cdot 10^{-5}$, $c_{120} = 8.7022 \cdot 10^{-3}$, $c_{021} = -2.9192 \cdot 10^{-3}$, $c_{102} = -2.1999 \cdot 10^{-5}$, $c_{012} = 9.0303 \cdot 10^{-5}$, $c_{220} = 3.3365 \cdot 10^{-5}$, $c_{202} = 9.4515 \cdot 10^{-8}$, $c_{022} = -2.6554 \cdot 10^{-5}$, $c_{030} = 0.67210$, $c_{130} = -9.0936 \cdot 10^{-3}$, $c_{031} = 6.9531 \cdot 10^{-4}$, $c_{040} = 4.8106 \cdot 10^{-2}$ and a fit quality of R^2=0.9999, SSE=$7.5565 \cdot 10^{-4}$, and RMSE=$2.5094 \cdot 10^{-3}$.

The normalized LM2500 $P^{max}_{fuel,ss}(\omega_{PT,ss})$ and $P^{min}_{fuel,ss}(\omega_{PT,ss})$ functions have the same third order polynomial form as given for the TSHAFT in Appendix A.3. However we note that, unlike the TSHAFT example, the data used to obtain $P^{max}_{fuel,ss}(\omega_{PT})$ and $P^{min}_{fuel,ss}(\omega_{PT})$ is taken from the GE simulator and thus $P_{out,ss}(P_{fuel,ss}, \omega_{PT,ss})$ is not required in this example. The data fit for $P^{max}_{fuel,ss}(\omega_{PT,ss})$ results in $c_{P^{max}_{fuel,ss}} = [1.7467, -1.1810 \cdot 10^{-2}, 5.1735 \cdot 10^{-4}, -2.9689 \cdot 10^{-6}]^T$ with R^2=0.9999, SSE=$1.9468 \cdot 10^{-5}$, and RMSE=$4.4113 \cdot 10^{-3}$. The data fit for $c_{P^{min}_{fuel,ss}} = [0.46995, 3.9101 \cdot 10^{-3}, -2.5088 \cdot 10^{-5}, 1.3044 \cdot 10^{-9}]^T$ with R^2=0.9998, SSE=$1.3289 \cdot 10^{-7}$, and RMSE=$3.6454 \cdot 10^{-4}$. Next, $\Delta_{P,f}$ is 1.7691 MW/s using Eq. (A.10) with the preceding fuel power functions and $\Delta t = 1.25$ s for an LM2500 [26].